Title:

Bridging of DNA breaks activate PARP2/HPF1 to modify chromatin

Authors:

Silvija Bilokapic[1], Marcin J. Suskiewicz[2], Ivan Ahel[2], Mario Halic*[1]

Affiliations:

[1]Department of Structural Biology, St. Jude Children's Research Hospital, 262 Danny Thomas Place, Memphis, TN, 38105, USA

[2]Sir William Dunn School of Pathology, University of Oxford, South Parks Road, Oxford OX1 3RE, UK

*Corresponding author

e-mail: mario.halic@stjude.org

Keywords:

DNA repair; PARP1; PARP2; HPF1; ADP-ribosylation; chromatin; histone modifications; cryo-EM

Summary:

DNA strand breaks recruit PARP1 and its paralogue PARP2 to modify histones and many other substrates with mono- and poly(ADP-ribose) (PAR)[1–5]. In DNA damage response, the PAR post-translational modification occurs predominantly on serine amino acids[6–8], which requires HPF1, an accessory factor that switches the amino-acid specificity of PARP1/2 from aspartate/glutamate to serine residues[9,10]. Poly(ADP) ribosylation (PARylation) is important for subsequent chromatin decompaction and serves as an anchor to recruit a variety of downstream signaling and repair factors to the sites of DNA breaks[2,11]. To understand the molecular mechanism of DNA break recognition by PARP enzymes in the context of chromatin, we determined cryo-EM structure of PARP2/HPF1 bound to a nucleosome. The structure shows that PARP2/HPF1 bridges two nucleosomes, with the broken DNA aligned in a ligation-competent position, revealing the initial step in double-strand DNA break repair. The bridging induces structural changes in PARP2 that signal DNA break recognition to the catalytic domain, which licenses HPF1 binding and PARP2 activation. Our data suggest that active PARP2 cycles through different conformational states to exchange NAD^+ and substrate, which may enable PARP enzymes to be processive while bound to chromatin. The mechanisms of PARP activation and catalytic cycle we describe can explain resistance mechanisms to PARP inhibitors, and will aid development of better inhibitors for cancer treatments[12–16].

PARP2/HPF1 bound to nucleosomes

To visualize the recognition of double-strand DNA lesions, we assembled the complex of PARP2/HPF1 bound to a mono-nucleosome, which mimics double-strand DNA break in a chromatin context (**Extended Data Fig. 1a-c**). In the electron micrographs, 2D class averages and initial 3D reconstructions we primarily observed two nucleosomes that are held together by an additional density bound at the DNA end of each nucleosome (**Extended Data Fig. 1d, e, 2a and Extended Data Table 1**). To improve the resolution of this flexible assembly, we have used focused classification followed by local search refinements. This improved the resolution of nucleosomes to 2.2 Å (Nucleosome 2) (**Extended Data Fig. 2b-d**) and 2.8 Å (Nucleosome 1) (**Extended Data Fig. 2e**), the density bridging two nucleosomes to 4.0 Å (**Extended Data Fig. 2f, g**) and PARP2/HPF1 to 3.9 Å (**Extended Data Fig. 3a-h**). All maps have sufficient overlapping densities to allow assembling a composite map and model (**Fig. 1a, b**).

In the structure, PARP2/HPF1 is located between two fully wrapped nucleosomes[17] and holds them together at the double-strand DNA break (**Fig. 1a, b**). This end-to-end DNA bridge is the only contact between the two nucleosomes. Two PARP2/HPF1 bind at the DNA break with their WGR domains (**Fig. 1a, b**); however, because of the flexibility of the entire complex, we have improved the resolution of one PARP2/HPF1. In a subset of data, nonetheless, both copies of the PARP2/HPF1 complex are present in a defined position (**Fig. 1c and Extended Data Fig. 4a-b**).

In the structure, the PARP2/HPF1 catalytic site, which is formed at the heterodimer interface[18], is positioned near the H3 N-terminal tails, ready to modify serine residues in the tails. Each PARP2/HPF1 is positioned to modify one of the H3 tails of the two neighboring nucleosomes (**Fig. 1b, c**).

PARP2/HPF1 bridges two nucleosomes

The PARP2 WGR domains bind a DNA break and hold two nucleosomes together (**Fig. 1d and Extended Data Fig. 4c-f**). In our data all such bridges are symmetrically bound by two WGR domains; however, a single WGR domain is capable of bridging the DNA break by simultaneously binding to the juxtaposed 5' phosphate (5'P) and 3' end of the broken DNA strand. In this assembly, two double-strand DNA breaks are brought together in a way that would facilitate a subsequent ligation. We do not observe direct interaction of two PARP2 enzymes, and two PARP2 WGR domains bind the break independently of each other. Binding of PARP2 WGR domains to nucleosomal DNA ends is consistent with a X-ray structure of an isolated PARP2 WGR domain bound to short DNA fragments[19] (**Extended Data Fig. 4e-f**).

In addition to the WGR domains, the PARP2 catalytic domain and HPF1 make several contacts with the nucleosomal and linker DNA. The HD loop connecting helices αD and αE of the PARP2 catalytic HD subdomain interacts with the linker DNA of the second nucleosome (**Fig. 1d**). In addition, HPF1 contacts the linker DNA of the same nucleosome through the positively charged residues in the helix α8, whereas positively charged residues in several loops make contacts with the nucleosomal DNA near the dyad and the entry/exit site (**Fig. 1d, e and Extended Data Fig. 4g**). In agreement with the structure, the complex with nucleosome is more stable than the complex with DNA, and HPF1 contributes to the complex stability (**Extended Data Fig. 5a, b**). Moreover, mutations of HPF1 residues that bind nucleosomal DNA destabilize HPF1 interaction with the PARP2_Nucleosome complex (**Extended Data Fig. 5c, d**). In the class with two PARP2/HPF1 bound to nucleosome, we observe an additional density that interacts with the DNA bridge and HPF1, which might be the N-terminal tail of PARP2[20] (**Extended Data Fig. 5e**).

We did not find a class in which PARP2 is not bound by HPF1, highlighting that when bound to a DNA break in a chromatin context these two proteins form a very stable complex. In the cryo-EM structure, PARP2 and HPF1 interact in a similar way to a recent crystal structure[18], with a slight rotation of HPF1 (**Extended Data Fig. 5f, g**). Notably, PARP2/HPF1 does not make any contacts with the histone core.

Bridging of DNA break activates PARP2

In our structure, the PARP2/HPF1 complex bridges two nucleosomes, implying that DNA bridging is required for PARP2 activation. To test this hypothesis, we have bound PARP2 to DNA which generated three distinct complexes: PARP2 bound to one DNA, one PARP2 bridging two DNAs and two PARP2 bridging two DNAs (**Fig. 2a and Extended Data Fig. 6a**). Adding NAD^+ to these complexes led to specific auto-PARylation of PARP2 that was bridging two DNAs (**Fig. 2a**). The assay also reveals that bridging of the DNA break by a single PARP2 is sufficient for triggering PARylation reaction, consistent with the observation that each WGR domain bridges independently the broken DNA strands (**Fig. 1d**).

While PARP2 forms a stable bridge with DNA bearing 5' P (**Fig. 1 and 2a**), the bridging is severely compromised upon loss of phosphates (**Extended Data Fig. 6b**). The bridged complex, however, shows similar PARylation activity when bound to both DNA, 5' P and 5' OH, indicating that weak PARylation of 5' OH DNA[19,21] is a result of inefficient DNA bridging (**Extended Data Fig. 6b-d**). Notably, in the bridged complex R140 makes an essential contact with the second nucleosome DNA, and its mutation abolishes complex formation and the H3 PARylation (**Fig. 1d, 2b and Extended Data Fig. 6e-g**). Our data show that bridging of the double-strand DNA break is required for PARP2 DNA-

dependent activation and that our structure represents the activated state of the PARP2/HPF1 complex.

We compared our cryo-EM structure of PARP2/HPF1 bound to nucleosomes with X-ray structures of PARP1 bound to DNA (PDB 4DQY), which represents a state prior to activation[22,23]. In our structure the hydrophobic and HD loops adopt a different conformation when compared to previous X-ray structures[22,24] (**Fig. 2c, Extended Data Fig. 7a-c and Supplementary Video 1**). The R140 in the WGR signaling loop interacts with the DNA of the second nucleosome, which pushes the loop that would otherwise clash with the bridged DNA, towards the hydrophobic loop connecting helices αB and αD in the HD subdomain (**Fig. 2c, d and Extended Data Fig. 7c**). The hydrophobic loop and the signaling loop move closer and form a hydrophobic pocket, in which V141 of the signaling loop interacts with the L254 and P253 in the hydrophobic loop (**Fig. 2c, e and Extended Data Fig. 7c, d**). Consequently, the K143 in the signaling loop interacts with D299 in the HD loop, which pushes the HD loop towards the DNA (**Fig. 2d and Extended Data Fig. 7d**)**.** Although mutation of V141 increased DNA-independent activation of PARP2, it abolished DNA-dependent H3 PARylation, consistent with its role in transmitting DNA binding to the active site (**Fig. 2b and Extended Data Fig. 6e-g**)**.** In agreement, mutations of two conserved leucines in the hydrophobic loop, result in DNA-independent activation of PARP1-3[21,22], indicating a conserved allosteric activation mechanism (**Extended Data Fig. 7f**).

The conformational changes in the interface between the WGR and the autoinhibitory HD subdomain lead to the rearrangement of the entire HD subdomain, particularly neighboring helices αA, αB and αF, which were previously shown to be important for auto-inhibition[23] (**Fig. 2c, Extended Data Fig. 7a-c and Supplementary Video 1**). In previous structures of the PARP1/2 catalytic domain (PDB 4TVJ), the HD subdomain helices clash with NAD^+ binding, indicating that the HD negatively regulates PARP activity[22,23] (**Fig. 2f and Extended Data Fig. 7g**). In our structure, however, helix αF in the HD subdomain moves away from the NAD^+ binding site, to a conformation in which residues E322 and D326 (D770 and D776 in PARP1) are compatible with NAD^+ binding[23,25] (**Fig. 2f**). This indicates that PARP2 in our structure is in activated conformation and can perform the catalytic reaction, in agreement with our biochemical assay (**Fig. 2a**).

Of note, HPF1 binding to PARP1 or PARP2 is inhibited by the HD subdomain and promoted by DNA and NAD^+ analogue binding[18], consistent with the idea that HPF1 will bind only the reaction-competent PARP conformations. In our structure rearrangement of helix αB of the HD subdomain alleviates the steric clash caused by E244 and opens the binding site for the interaction with HPF1 (**Fig. 2g**). In

agreement, we observe that HPF1 binds only the active complex that bridges two DNA molecules (**Fig. 2h**).

In summary, the structure shows that bridging two nucleosome rearranged the signaling loop in the WGR domain and reveals mechanistic basis for signal propagation from recognition of DNA damage to changes in the autoinhibitory HD subdomain and PARP activation.

PARP2/HPF1 catalytic cycle

The structure of activated PARP2/HPF1 reveals conformational changes that would allow for NAD^+ binding and, consequently, the ADP-ribosylation reaction; however, bound NAD^+ would be buried between PARP2 and HPF1 and may not be readily exchanged (**Fig. 3a**). Beside the most stable active conformation of the PARP2/HPF1 complex, we have solved two distinct structures of more dynamic states of PARP2/HPF1 (**Extended Data Fig. 3c, d**).

In the first structure, we found that two helices of the PARP2 HD subdomain, αD and αF, and active site loop, ASL or D-loop, are flexible (**Fig. 3a, b and Extended Data Fig. 8a-c**). This is consistent with HX-MS data, showing that αD, αF and ASL have high exchange of hydrogen-deuterium after DNA-dependent activation of PARP1[23] (**Extended Data Fig. 8d**). In our structure delocalization of these helices and the ASL loop generates a large opening between the PARP2 HD and ART catalytic subdomains (**Fig. 3b and Extended Data Fig. 8e**). In the activated conformation, modeled NAD^+ is buried, which implicates that either the complex needs to dissociate before the next ADP-ribose can be added, or the complex cycles through conformational changes that allow for NAD^+ binding and product release. In the state with delocalized ASL, αD and αF, the large opening could be used for NAD^+ binding and exchange (**Fig. 3b, Extended Data Fig. 8e, f**). The ability of PARPs to exchange NAD^+, without the necessity to release the substrate, would make PARPs processive enzymes that can add chains of ADP-ribose while holding on to the substrate.

The model of the H3 tail bound to the activated PARP2/HPF1 complex shows that the H3 tail could access this conformation and catalysis could occur; however, the product containing large ADP-ribose would be buried between PARP2 and HPF1 (**Extended Data Fig. 9a**). We have solved a structure of another distinct intermediate state in which we observe flexibility of two different helices in the PARP2 HD subdomain, αB and the N-terminal part of αD, as well as two HPF1 helices, α7 and α8 (**Fig. 3a, c and Extended Data Fig. 9b-d**). The delocalization of PARP2 helices αB and αD is also in agreement with HX-MS data for PARP1[23] (**Extended Data Fig. 8d**). This structural change generates a large opening between PARP2 HD subdomain and HPF1 which could be used for the product release (**Fig. 3c and Extended Data Fig. 9e-f**), whereas NAD^+ exchange site remains closed (**Extended Data Fig.**

9d). The ability to release the product would enable PARP/HPF1 to modify multiple substrates, without the need to disassemble.

These structures suggest that PARPs could cycle between states in which they would exchange NAD^+, perform catalytic reaction and release the product. This would allow the PARP/HPF1 complex to bind and modify multiple substrates, while remaining bound to, and thus protecting, the chromatin lesion (**Extended Data Fig. 10a**). The enzymatic cycle we describe is consistent with previous biophysical data obtained with PARP1[23], and might be applicable to all DNA-dependent PARPs and perhaps to other ADP-ribosylating enzymes.

Auto-PARylation dissociates the complex

To examine the effects of PARylation on the interactions with the chromatin, we have initiated the reaction by adding NAD^+ to the assembled PARP2/HPF1_Nucleosome complex and observed that PARP2 modified histone H3, HPF1 and itself (**Fig. 4a, b**). This resulted in PARP2/HPF1 dissociation from the nucleosome and produced PARylated nucleosomes (**Fig. 4a, b**). The kinetic of the reaction shows that H3 is PARylated very rapidly, and that longer incubation does not lead to a major increase in the H3 PARylation, indicating that most H3 tails were modified immediately after activation (**Fig. 4c, d**). Notably, the complex remains stably bound to the nucleosome at this point (**Fig. 4c, d**). In contrast, PARP2 auto-PARylation increases with time and eventually destabilizes the entire complex (**Fig. 4a-d**). These data show that PARP2/HPF1 will rapidly modify histones that serve as a recruitment platform for other factors involved in DNA repair. The reaction will slowly switch from histone PARylation to auto-PARylation, which leads to gradual dissociation of PARP2/HPF1 from chromatin (**Fig. 4c, d**), in agreement with previous observations[21,26,27]. The delay in auto-PARylation kinetics and slow release from chromatin opens a window of opportunity for recruitment of DNA repair factors[2,4], while PARPs remain bound to chromatin, bridging across the DNA break. This ensures that broken, but bridged DNAs can be passed to new set of factors, such as ligases, that will repair the break (**Extended Data Fig. 10b, c**).

Discussion

Catalytic site inhibitors of PARP enzymes are efficiently used in cancer therapies, however, resistance to PARP inhibitors is becoming an increasingly relevant issue[28] (**Extended Data Fig. 10d**). In a patient with resistance to olaparib, the R591C mutation was identified in PARP1 (R140 in PARP2)[29], which was shown to break signaling between the WGR and the catalytic domains[30]. In agreement, we find that mutation of this residue abolishes nucleosome binding and bridging (**Fig. 1d and 2b**), which might explain *in vivo* observation that this mutant is not trapped, but rapidly dissociates from chromatin[29].

Similarly, talazoparib resistant mutation in PARP1[29], the HD742-743F (HD298-299 in PARP2) is located in the HD loop (**Fig. 2d**), which interacts with the second nucleosome DNA. This mutation might disrupt the HD loop interactions, providing a plausible explanation for observed loss of trapping[29]. Another mutation that leads to inhibitor resistance is a deletion of VE687-688 in PARP1[29] (VE243-244 in PARP2). This residues regulate PARP activation and HPF1 binding (**Fig. 2g**), indicating that in these cancer cells PARP/HPF1 might be constitutionally active, which could counteract inhibition.

The mechanisms of PARP activation and PARP catalytic cycle we describe in this study provide better understanding why these mutations found in PARP enzymes cause the resistance to inhibitors, and will have important contribution to development of better PARP inhibitors for cancer treatments.

253 **References**

1. Liu, C., Vyas, A., Kassab, M. A., Singh, A. K. & Yu, X. The role of poly ADP-ribosylation in the first wave of DNA damage response. *Nucleic Acids Res.* **45**, 8129–8141 (2017).
2. Ray Chaudhuri, A. & Nussenzweig, A. The multifaceted roles of PARP1 in DNA repair and chromatin remodelling. *Nat. Rev. Mol. Cell Biol.* **18**, 610–621 (2017).
3. Gupte, R., Liu, Z. & Kraus, W. L. PARPs and ADP-ribosylation: recent advances linking molecular functions to biological outcomes. *Genes Dev.* **31**, 101–126 (2017).
4. Caldecott, K. W. Protein ADP-ribosylation and the cellular response to DNA strand breaks. *DNA Repair (Amst.)* **19**, 108–113 (2014).
5. Pascal, J. M. The comings and goings of PARP-1 in response to DNA damage. *DNA Repair (Amst.)* **71**, 177–182 (2018).
6. Leidecker, O. *et al.* Serine is a new target residue for endogenous ADP-ribosylation on histones. *Nat. Chem. Biol.* **12**, 998–1000 (2016).
7. Bonfiglio, J. J. *et al.* Serine ADP-Ribosylation Depends on HPF1. *Mol. Cell* **65**, 932-940.e6 (2017).
8. Larsen, S. C., Hendriks, I. A., Lyon, D., Jensen, L. J. & Nielsen, M. L. Systems-wide Analysis of Serine ADP-Ribosylation Reveals Widespread Occurrence and Site-Specific Overlap with Phosphorylation. *Cell Rep* **24**, 2493-2505.e4 (2018).
9. Gibbs-Seymour, I., Fontana, P., Rack, J. G. M. & Ahel, I. HPF1/C4orf27 Is a PARP-1-Interacting Protein that Regulates PARP-1 ADP-Ribosylation Activity. *Mol. Cell* **62**, 432–442 (2016).
10. Palazzo, L. *et al.* Serine is the major residue for ADP-ribosylation upon DNA damage. *Elife* **7**, (2018).
11. Ciccia, A. & Elledge, S. J. The DNA damage response: making it safe to play with knives. *Mol. Cell* **40**, 179–204 (2010).
12. Bryant, H. E. *et al.* Specific killing of BRCA2-deficient tumours with inhibitors of poly(ADP-ribose) polymerase. *Nature* **434**, 913–917 (2005).
13. Farmer, H. *et al.* Targeting the DNA repair defect in BRCA mutant cells as a therapeutic strategy. *Nature* **434**, 917–921 (2005).

14. Hou, W.-H., Chen, S.-H. & Yu, X. Poly-ADP ribosylation in DNA damage response and cancer therapy. *Mutat. Res.* **780**, 82–91 (2019).
15. Lord, C. J. & Ashworth, A. PARP inhibitors: Synthetic lethality in the clinic. *Science* **355**, 1152–1158 (2017).
16. Murai, J. *et al.* Trapping of PARP1 and PARP2 by Clinical PARP Inhibitors. *Cancer Res.* **72**, 5588–5599 (2012).
17. Bilokapic, S., Strauss, M. & Halic, M. Histone octamer rearranges to adapt to DNA unwrapping. *Nat. Struct. Mol. Biol.* **25**, 101–108 (2018).
18. Suskiewicz, M. J. *et al.* HPF1 completes the PARP active site for DNA damage-induced ADP-ribosylation. *Nature* **579**, 598–602 (2020).
19. Obaji, E., Haikarainen, T. & Lehtiö, L. Structural basis for DNA break recognition by ARTD2/PARP2. *Nucleic Acids Res.* **46**, 12154–12165 (2018).
20. Riccio, A. A., Cingolani, G. & Pascal, J. M. PARP-2 domain requirements for DNA damage-dependent activation and localization to sites of DNA damage. *Nucleic Acids Res.* **44**, 1691–1702 (2016).
21. Langelier, M.-F., Riccio, A. A. & Pascal, J. M. PARP-2 and PARP-3 are selectively activated by 5’ phosphorylated DNA breaks through an allosteric regulatory mechanism shared with PARP-1. *Nucleic Acids Res.* **42**, 7762–7775 (2014).
22. Langelier, M.-F., Planck, J. L., Roy, S. & Pascal, J. M. Structural basis for DNA damage-dependent poly(ADP-ribosyl)ation by human PARP-1. *Science* **336**, 728–732 (2012).
23. Dawicki-McKenna, J. M. *et al.* PARP-1 Activation Requires Local Unfolding of an Autoinhibitory Domain. *Mol. Cell* **60**, 755–768 (2015).
24. Thorsell, A.-G. *et al.* Structural Basis for Potency and Promiscuity in Poly(ADP-ribose) Polymerase (PARP) and Tankyrase Inhibitors. *J. Med. Chem.* **60**, 1262–1271 (2017).
25. Langelier, M.-F., Zandarashvili, L., Aguiar, P. M., Black, B. E. & Pascal, J. M. NAD+ analog reveals PARP-1 substrate-blocking mechanism and allosteric communication from catalytic center to DNA-binding domains. *Nat Commun* **9**, 844 (2018).

26. Kim, M. Y., Mauro, S., Gévry, N., Lis, J. T. & Kraus, W. L. NAD+-dependent modulation of chromatin structure and transcription by nucleosome binding properties of PARP-1. *Cell* **119**, 803–814 (2004).
27. Muthurajan, U. M. *et al.* Automodification switches PARP-1 function from chromatin architectural protein to histone chaperone. *Proc. Natl. Acad. Sci. U.S.A.* **111**, 12752–12757 (2014).
28. Yap, T. A., Plummer, R., Azad, N. S. & Helleday, T. The DNA Damaging Revolution: PARP Inhibitors and Beyond. *Am Soc Clin Oncol Educ Book* **39**, 185–195 (2019).
29. Pettitt, S. J. *et al.* Genome-wide and high-density CRISPR-Cas9 screens identify point mutations in PARP1 causing PARP inhibitor resistance. *Nat Commun* **9**, 1849 (2018).
30. Zandarashvili, L. *et al.* Structural basis for allosteric PARP-1 retention on DNA breaks. *Science* **368**, (2020).

Fig. 1. PARP2/HPF1 bridges two mono-nucleosomes.

a) Composite cryo-EM map of PARP2/HPF1 bound to 5'-phosphorylated nucleosome at 2.1-3.9 Å resolution.

b) Model for the cryo-EM structure of PARP2/HPF1 bound to bridged mono-nucleosomes.

c) Model for the cryo-EM map with two PARP2/HPF1 bound to bridged mono-nucleosomes. Two PARP2/HPF1 are positioned to modify H3 on opposite sides of nucleosomes.

d) View at the bridge with two PARP2 WGR domains connecting two nucleosomes containing a double-strand DNA break. Two DNAs are positioned in a way that the 5'P of the Nucleosome 1 DNA is aligned with the 3'OH group of the Nucleosome 2 DNA, and vice versa. PARP2 catalytic domain binds the linker DNA with the loop in the HD subdomain (CAT_HD). HPF1 binds the linker DNA through the helix α8.

e) HPF1 binds nucleosomal DNA near the dyad with several positively charged residues in the N-terminal domain.

Fig. 2. Bridging of DNA break activates PARP2.

a) In-gel PARylation assay. PARP2 was bound to DNA and distinct complexes were separated: PARP2 bound to one DNA, one PARP2 bridging two DNAs and two PARP2 bridging two DNAs (note stronger PARP2 signal in the upper band). Gel was incubated with NAD^+ and ADP-ribosylation was detected.

b) Activity of wild type and mutant PARP2 on the nucleosome detected by SDS-PAGE/immunoblotting .

c) Structural alignment of WGR domains of the nucleosome bound PARP2 (violet) and the DNA bound PARP1 (gray, PDB: 4DQY). The signaling loop, as in PARP1_WGR, would clash with the second DNA (red mark).

d) Close-up view of the signaling loop (aa:139-145) interactions with DNA, the hydrophobic loop (aa:248-258) and the HD loop (aa:297-310).

e) Close-up view of the PARP2 hydrophobic pocket formed by the hydrophobic loop, the signaling loop and the HD loop. V141 in the signaling loop interacts with L254 and P253 of the hydrophobic loop.

f) Close-up view of the nucleosome bound PARP2 (violet) superimposed to the PARP2 crystal structure (gray, PDB:4TVJ). Rearrangement of the HD subdomain alleviates the steric clash with NAD^+.

g) X-ray structure of the PARP2 catalytic domain (gray, PDB:4TVJ) was superimposed on the cryo-EM structure of PARP2/HPF1. HPF1 clashes with the PARP2 E244 in its inactive conformation (gray, PDB:4TVJ). Rearrangement of PARP2 αB enables HPF1 binding.

h) In-gel PARylation assay as in **a)**: HPF1 binds only PARP2 that bridged two DNAs.

One representative of at least 3 independent biochemical experiments is shown. For gel source data, see Supplementary Fig. 1.

Fig. 3. PARP2 catalytic domain rearranges to open NAD^+ and substrate binding sites.

a) View at the active site formed by PARP2 and HPF1 in the nucleosome bound activated conformation.

b) View at the active site formed by PARP2 and HPF1 in the nucleosome bound open state 1. PARP2 helices αF, αD and active site loop (ASL) are flexible, which might open active site for NAD^+ binding.

c) View at the active site formed by PARP2 and HPF1 in the nucleosome bound open state 2. Dislocation of PARP2 helices αD and αB, and HPF1 helices α7 and α8, might open substrate release pocket.

NAD^+ (yellow) was modeled based on an alignment with PDB:6BHV.

Fig. 4. PARylated PARP2/HPF1 dissociate from the chromatin.

a) Assembled PARP2/HPF1_Nucleosome complex was incubated with and without NAD^+ and analyzed by EMSA. Note the shift in the position of PARylated nucleosomes in respect to the unmodified nucleosomes. PARylated PARP2 does not co-migrate with PARylated nucleosomes, indicating dissociation.

b) SDS-PAGE/immunoblotting of the reaction in **a)**. The complex activation leads to ADP-ribosylation of H3.

c) The changes in the PARP2/HPF1_Nucleosome complex during PARylation reaction were followed by EMSA. Initial PARylation does not lead to the complex dissociation; however, longer PARylation dissociates the complex and generates PARylated nucleosomes.

d) The extent of the PARylation reaction was followed by PAGE/immunoblotting. In the first steps, H3, HPF1 and PARP2 are PARylated to similar extent. Extended reaction (60 min) leads to increase in PARP2 auto-PARylation.

One representative of at least 3 independent biochemical experiments is shown. For gel source data, see Supplementary Fig. 1.

Experimental Procedures

Histone expression and purification

Xenopus laevis histones were individually over-expressed in BL21(DE3) pLysS bacterial strain and purified from the inclusion bodies, as described[31]. Transformed *E. coli* cells were grown in LB medium at 37 °C until the OD_{600nm} reached 0.6. Protein expression was induced by addition of 1 mM IPTG for 3 hours at 37 °C. Pelleted cells were frozen, resuspended in lysis buffer (50 mM Tris-HCl, pH 7.5, 150 mM NaCl, 1 mM EDTA, 1 mM DTT, 0.1 mM PMSF) and sonicated. The pellet containing inclusion bodies was isolated by centrifugation for 20 min at +4 °C and 35 000 rcf, resuspended in the lysis buffer supplemented with 1% Triton X-100 and spun down. The wash step was repeated two times with the buffer containing 1% Triton X-100 and subsequently two times with buffer without Triton X-100. The insoluble pellet, containing histone protein, was retrieved by centrifugation after each solubilization step.

Each histone protein was extracted from the purified inclusion body pellet in a buffer containing 50 mM Tris, 7.5, 2 M NaCl, 6 M guanidine hydrochloride, 1 mM DTT for 1 hour at room temperature. Any insoluble components were removed by centrifugation. Proteins making histone pairs (H2A and H2B, H3 and H4) were combined in equimolar ratios and dialysed two times in 1l of refolding buffer (25 mM HEPES/NaOH, pH 7.5, 2 M NaCl, 1 mM DTT) at +4 °C. Any precipitate was removed by centrifugation for 20 min, 35 000 rcf at +4 °C. The soluble histone pairs were further purified via cation-exchange chromatography in batch (SP Sepharose Fast Flow resin). The samples were diluted four fold with buffer without salt (25 mM HEPES/NaOH, pH 7.5 and 1 mM DTT) and bound to the resin for 15-20min. The resin was extensively washed with 500 mM salt buffer in batch (25 mM HEPES/NaOH, pH 7.5, 500 mM NaCl and 1 mM DTT) and loaded onto a disposable column. On the column, the resin was washed and pure proteins were eluted with 25 mM HEPES/NaOH, pH 7.5, 2 M NaCl, 1 mM DTT. Soluble histone pairs were concentrated and purified on the size exclusion column equilibrated in 25 mM HEPES/NaOH, pH 7.5, 2 M NaCl, 1 mM DTT. Clean protein fractions were pooled, concetrated and flash frozen.

Histone octamer preparation

Histone octamer was prepared as described previously[32,33]. To obtain the histone octamer a 2.5 fold excess of H2A/H2B histone dimer was mixed with H3/H4 histone tetramer. The access of H2A/H2B dimer was purified from the histone octamer by the size exclusion chromatography (Superdex 200 Increase 10/300 GL) that has been pre-equilibrated in 25 mM HEPES/NaOH pH 7.5, 2 M NaCl, 1 mM

DTT. The fractions with the protein were analysed on SDS-PAGE, concetrated and used in nucleosome assembly (**Extended Data Fig. 1a**).

Nucleosomal DNA preparation

Nucleosomal DNA was PCR amplified from a plasmid harboring the 147 base pair 601 DNA sequence[34]. Primers, containing 5' P, with various length of overhangs were designed, used for DNA amplification and nucleosome assembly.

Nucleosome assembly

Nucleosome assembly was done by 'double bag' dialysis, as described[33,35]. Nucleosomal DNA was resuspended in 25 mM HEPES/NaOH pH 7.5, 2 M NaCl, 1 mM DTT. The histone octamer, after size exclusion chromatography purification, was mixed with DNA and placed into a dialysis button (membrane cutoff 3.5 kDa MW). The dialysis buttons were placed inside a dialysis bag (membrane cutoff 6-8 kDa MW), filled with 50 ml of buffer containing 25 mM HEPES/NaOH pH 7.5, 2 M NaCl, 1 mM DTT. The dialysis bag was immersed into a 1l of buffer containing 15 mM HEPES/NaOH pH 7.5, 1M NaCl, 1 mM DTT and dialysed over-night at + 4 °C. The next day the dialysis bag was immersed into a 1l of buffer containing 15 mM HEPES/NaOH pH 7.5, 50 mM NaCl, 1 mM DTT and dialysed for 5–6 hours. Finally dialysis buttons were removed from the dialysis bag and dialysed for 1 hour into a fresh buffer containing 50 mM NaCl. Quality of the reconstituted nucleosomes was assessed by 6% native PAGE, run in 1 x TBE, 200 V, + 4 °C. The gel was stained by SYBR Gold (**Extended Data Fig. 1b**).

Cloning Procedures

All mutant constructs were made by inverse PCR (iPCR) using plasmids that contained the gene for the full-length protein: HPF1 (UniProt Q9NWY4) and PARP2 (UniProt Q9UGN5-2). iPCR reactions were set up in a total volume of 25 µl. 10 µl of purified PCR product was incubated with 5 U of T4 PNK in 20 µl of 1× T4 DNA ligase buffer for 1 h at 37°C. 200 U of T4 DNA ligase was added to the reaction and incubated for 1 h at room temperature. Finally, 10 U of DpnI was added to the reaction and incubated for 1h at 37°C. 5 µl was used to transform the competent XL1-Blue *E. coli* cells. All plasmid sequences were verified by DNA sequencing. Oligos are listed in **Supplementary Table 1**.

Purification of PARP2 and HPF1

E. coli LOBSTR Rosetta bacterial culture, containing pET28 vector harboring wild type or desired PARP2 or HPF1 mutation, was grown in LB medium containing the appropriate antibiotics at 37 °C until the optical density reached 0.6 at 600 nm. PARP2 toxicity was prevented by adding 10 mM benzamide. The culture was shifted to 18 °C for 30 min and induced with 0.2 mM IPTG. Harvested

cells, after overnight induction at 18 °C, were resuspended in lysis buffer (30 mM HEPES/NaOH, pH 8.0, 2 M NaCl, 20 mM imidazole, 3 mM β-mercaptoethanol, 0.1 mM PMSF, 2.5 U/ml benzonase) and lysed. Proteins from the cleared supernatant were affinity-purified using Ni Sepharose 6 Fast Flow resin. After binding, the resin was extensively washed with lysis buffer in batch and loaded onto a disposable column. On the column, the resin was washed with 4 bed volumes of washing buffer (30 mM HEPES/NaOH, pH 8.0, 2 M NaCl, 40 mM imidazole, 3 mM β-mercaptoethanol) and the bound protein was eluted with 4 bed volumes of elution buffer (30 mM HEPES/NaOH, pH 8.0, 2 M NaCl, 300 mM imidazole, 3 mM β-mercaptoethanol). The proteins were dialyzed against 30 mM HEPES/NaOH, pH 7.5, 100 mM NaCl, 0.1 mM EDTA, 1 mM DTT and further purified on HiTrap Heparin column using linear NaCl gradient . The fractions with the protein were concentrated and applied on size exclusion Superdex 200 Increase 10/300 equilibrated in 20 mM HEPES/NaOH, pH 7.5, 200 mM NaCl, 1 mM DTT. The fractions with the protein were analysed on SDS-PAGE and concetrated (**Extended Data Fig. 5c and 6e**).

Assembly of the PARP2/HPF1_Nucleosome complex for cryo-EM analysis

Nucleosomes, at final concentration not exceeding 0.3 μM, were assembled by 'double bag' dialysis with the second dialysis buffer containing 15 mM HEPES/NaOH pH 7.5, 300 mM NaCl, 1 mM DTT. 0.5 molar equivalents of PARP2 and 2 molar equivalents of HPF1 were added to the nucleosome sample and dialysis was continued into the final dialysis buffer containing 15 mM HEPES/NaOH pH 7.5, 50 mM NaCl, 1 mM DTT. In order to avoid the sample precipitation, nucleosomes and PARP2/HPF1 proteins were mixed at elevated salt concentration and gradually dialysed into 50mM salt buffer. The formation of PARP2/HPF1_Nucleosome complex was monitored by native PAGE (**Extended Data Fig. 1b**). Samples containing linker DNA shorter than 6bp showed severe precipitation during complex preparation. Each soluble PARP2/HPF1_Nucleosome complex, containing different length of nucleosomal linker DNA, was used for cryo-EM grid preparation. The optimal length of the linker DNA, for structural studies of this complex contained 10 bp linker arm on both sides of a centrally positioned 601 sequence.

DNA bridging assay

167bp DNA containing 601 Widom sequence with 5' P on the one end and 5' biotin on the other end was used for the PARP2 bridging assay. Incorporation of biotin prevented continuous DNA end joining and formation of ladder of PARP2/DNA complex species on the native gel. As a control, incorporation of 5' biotin on both DNA ends efficiently blocked dimerization of DNA by PARP2 (**Extended Data Fig. 6a**). Binding of PARP2 to DNA having 5' P on one end and biotin on the opposite end generated three

distinct complexes separated on a native gel: PARP2 bound to one DNA, one PARP2 bridging two DNAs and two PARP2s bridging two DNAs. 0.34 μM DNA was mixed with 0.1 μM PARP2 in the final buffer containing 15 mM HEPES/NaOH pH 7.5, 150 mM NaCl, 1 mM DTT at + 4 °C for 1h. The influence of HPF1 on DNA bridging by PARP2 was evaluated by adding 0.2 μM HPF1 into the reaction. 4% glycerol with bromophenol blue was added to the samples before the analysis on 6% native PAGE. The gel was run in 1 x TBE, 200 V, + 4 °C, stained by SYBR Gold and imaged. The gel was briefly washed in buffer containing 15 mM HEPES/NaOH pH 7.5, 150 mM NaCl, 1 mM DTT and incubated in the same buffer supplemented with NAD^+ for 1 or 5 min. The PARylation reaction was stopped by incubating the gel in 1xSDS running buffer for 10-15min. This step was also required to denature proteins for subsequent Western blot detection.

DNA hairpin was refolded by incubating for 10 min at + 95 °C at 10 μM DNA concentration. DNA bridging assay with DNA hairpin was done with 0.8 μM 24 bp DNA hairpin, with and without 5' phosphate, and 0.2, 0.3, 0.4 and 0.5 μM PARP2 and incubated for 30 min at room temperature in 30 mM HEPES/NaOH pH 7.5, 80mM NaCl, 1 mM DTT. Samples were analyzed on 6% native PAGE. The gel was run in 1 x TBE, 200 V, + 4 °C for 70min to get separation of PARP2:DNA hairpin complexes. Due to the small size of DNA hairpin they run out of 6% native gel when not in the complex with PARP2. The gel was stained with SYBR Gold and the PARylation reaction was done by incubating the gel for 7 min in 15 mM HEPES/NaOH pH 7.5, 50 mM NaCl, 1 mM DTT, 150 μM NAD^+.

Competitive binding assay

Free DNA is stained significantly better by DNA intercalation dye than DNA incorporated into the nucleosome and quantification of these two species is not possible by this method. Thus, we have prepared 167bp DNA containing 601 Widom sequence with 5' P on the one end and 5' Alexa Fluor 488 dye on the other end. Alexa Fluor 488 labeled DNA was used for the nucleosome assembly. Equimolar amounts of free Alexa488-DNA and Alexa488-nucleosomes were incubated with increasing amounts of PARP2 and HPF1 and loaded on 6% native PAGE. Intrinsic excitation of Alexa Fluor 488 dye was used to analyze the competitive binding assay.

Western blot detection

SDS-PAGE gels or native PAGE gels, after denaturation in 1xSDS running buffer, were transferred to PVDF membrane and blocked in TBST (50 mM Tris/HCl, pH 7.5, 150 mM NaCl, 0.1% tween-20) containing 5% milk for 1 h. Membranes were then incubated in primary antibody in TBST containing 5% milk for 1 h at room temperature. The membranes were washed 3 x for 5 min with TBST and incubated in secondary antibody for 1 h at room temperature. Membranes were washed for 3 x 5 min

with TBST before chemiluminescent detection. Antibodies used include PARP2 (Enzo Life Sciences, ALX-804-639-L001), H3 (AbCam, ab1791), HRP-conjugated anti-rabbit secondary antibody (Biorad, 170-6515), HRP-conjugated anti-mouse secondary antibody (Biorad, 170-6516) and anti-poly-ADP-ribose binding reagent (Sigma-Aldrich, MABE1016).

Native gel-shift assays with PARP2 and HPF1 mutants

To prevented continuous nucleosome end joining due to PARP2 binding and formation of a ladder of complex species on the native gel, nucleosomes were assembled with 167bp DNA containing 5' P on the one end and 5' biotin on the other end. 0.07 µM nucleosomes were incubated with 0.15 µM PARP2, wild type or mutant, and 0.3 µM HPF1, wild type or mutant, for 30 min at room temperature in 30 mM HEPES/NaOH pH 7.5, 50mM NaCl, 1 mM DTT. In the binding assay with PARP2 mutants, binding to the nucleosome was tested with and without wild-type HPF1. In the binding assay with HPF1 mutants two different salt concentrations were tested: 50mM, as used for cryo-EM analysis, and 125mM NaCl, closer to the physiological level.

ADP-ribosylation assay

PARP2 and HPF1 were pre-mixed for 1h at + 4 °C in 15 mM HEPES/NaOH pH 7.5, 50 mM NaCl, 1 mM DTT at concentrations of 2.6 µM PARP2 and 10 µM HPF1. This mixtures was treated as a 10x enzyme mix and incubated with 0.25 µM nucleosomes in 15 mM HEPES/NaOH pH 7.5, 50 mM NaCl, 1 mM DTT at + 4 °C for 1h. 150 µM NAD^+ was added to the complex sample and incubated for additional 1h at + 30 °C. The samples without added NAD^+ were in parallel incubated at + 30 °C. The reactions were analyzed on 6% native PAGE and stained by SYBR Gold. Subsequently, an antibody for histone H3 and for PARP2 was used for Western detection of the samples separated on the native gel. The extent of PARylation reaction was also followed on SDS-PAGE by Western detection with H3 antibody and anti-poly-ADP-ribose binding reagent. Two control reactions, nucleosomes incubated only with PARP2 or only with HPF1, showed no H3 PARylation (**Extended Data Fig. 1c**). ADP-ribosylation assay with PARP2 mutants, PARP2_V141D and PARP2_R140A, was done using 0.1 µM wild type and mutant PARP2 for 1h at + 30 °C. The reaction was analyzed by Western detection after SDS-PAGE.

Time course of the ADP-ribosylation reaction was followed using the PARP2/HPF1_Nucleosome sample prepared for cryo-EM analysis. The sample was incubated with 150 µM NAD^+ at + 30 °C for different amounts of time as labeled in the **Fig. 4c, d**. The reaction was loaded on 6% native and SDS-

PAGE gel. The native gel was stained with SYBR Gold. Anti-poly-ADP-ribose binding reagent was used for detection of PAR chains separated on SDS-PAGE.

SDS-PAGE PARP2 automodification assay

The SDS-PAGE PARP2 automodification assay was performed essentially as described[22]. 0.5 µM PARP2 wild type and mutants were preincubated with 1 µM 24 bp DNA hairpin in 30 mM HEPES/NaOH pH 7.5, 50 mM NaCl, 1 mM DTT, 1.5 mM $MgCl_2$ for 30 min at room temperature. 150 µM NAD+ was added to the reaction and incubated for 10 min at + 30 °C. Reaction with DNA hairpin, with and without 5' phosphate, and wt PARP2 were incubated for 30 min at + 30 °C. The reaction was quenched by the addition of SDS loading buffer. The samples were run on SDS-PAGE and stained with SimplyBlue SafeStain.

CryoEM grid preparation and data collection

For cryo-EM we have assembled PARP2/HPF1_Nucleosome complex as described. The sample was concentrated to 0.25 mg/ml for cryo-EM grid. To avoid the extensive aggregation of the complex sample on the cryo-EM grid, PARP2 was mixed with nucleosomes in substoichiometric amounts. 3 µl of PARP2/HPF1_Nucleosome complex sample were applied to freshly glow-discharged Quantifoil R2/1 holey carbon grid. Humidity in the chamber was kept at 95% and temperature at + 10 °C. After 5 s blotting time, grids were plunge-frozen in the liquid ethane using FEI Vitrobot automatic plunge freezer.

Electron micrographs were recorded on FEI Titan Krios at 300 kV with a Gatan Summit K3 electron detector (~20000 micrographs) at the Cryo-EM facility at St. Jude Childrens's Research Hospital. Image pixel size was 1.06 Å per pixel on the object scale. Data were collected in a defocus range of 7 000 Å – 30 000 Å with a total exposure of 90 e/Å^2. 50 frames were collected and aligned with the MotionCorr2 software using a dose filter[36,37]. The contrast transfer function parameters were determined using CTFFIND4[38].

Several thousand particles were manually picked and used for training and automatic particle picking in Cryolo[39]. Particles were windowed and 2D class averages were generated with the Relion software package[40]. Inconsistent class averages were removed from further data analysis. The initial reference was filtered to 40 Å in Relion. C1 symmetry was applied during refinements for all classes. Particles were split into 2 datasets and refined independently and the resolution was determined using the 0.143 cut-off (Relion auto refine option). All maps were filtered to resolution using Relion with a B-factor determined by Relion.

Initial 3D refinement was done with 943 000 particles. To improve the resolution of this flexible assembly, we have used focused classification followed by focused local search refinements. Nucleosome 1 and 2 were refined with all particles. Nucleosome 2 was centered and refined to 2.2 Å, reaching the Nyquist limit. Nucleosome 1 was refined off center, reaching 2.8 Å. Connection between Nucleosome 1 and PARP2 (bridge) was refined to 6.3 Å using all particles. Connection between Nucleosome 2 and PARP2 (bridge) was classified and refined to 4.0 Å. PARP2/HPF1 containing bridge DNA was centered and extensively classified. Due to the flexibility of PARP2/HPF1 bound to chromatin, the most stable active conformation of PARP2/HPF1 with bridge DNA was refined to 4.2 Å using 32 000 particles. The flexible bridge DNA was removed from further classification and refinements, which improved the resolution to 3.9 Å using 17 000 particles. Two more dynamic intermediate states were classified and the resolution was improved to 6.3 Å and 6.7 Å, using with 9 500 and 11 000 particles respectively. In a subset of data, which includes 140 000 particles, we see densities for both PARP2/HPF1 bridging two mono-nucleosomes. For final reconstruction of this map 16 000 particles was used. All maps have extensive overlapping densities that we used to assemble the composite map and model. Directional FSC was calculated using 3DFSC server[41].

Molecular models were built using Coot[42]. The model of the NCP (PDB:6FQ5)[33] was refined into the cryo-EM map of Nucleosome 1 and Nucleosome 2 with linker DNA manually built in Coot and geometry optimized with base pairing and base stacking restraints in PHENIX[43]. The model of the PARP2_WGR domain (PDB:6F5B)[19], PARP2 catalytic domain (PDB:4TVJ)[24] and PARP2 catalytic domain (without HD subdomain) in complex with HPF1 (PDB:6TX3)[18] were rigid-body placed using PHENIX, manually adjusted and re-build in COOT and refined in Phenix. Visualization of all cryo-EM maps was done with Chimera[44].

Acknowledgments

We would like to thank Alexander Myasnikov and Liang Tang from the Cryo EM facility at St. Jude Children's Research Hospital for support with the data collection. M.J.S. is supported by EMBO Long-term Fellowship ALTF 879-2017. Work in Ivan Ahel's laboratory is funded by the Wellcome Trust [grant numbers 101794 and 210634], BBSRC [BB/R007195/1] and Cancer Research UK [C35050/A22284]. Work in Halic's laboratory is funded by St. Jude Children's Research Hospital, the American Lebanese Syrian Associated Charities and NIH award 1R01GM135599-01.

Author contributions

S.B. and M.H. designed the experiments. M.J.S purified wild type PARP2 and HPF1 for cryo-EM analysis. S.B. cloned and purified PARP2 and HPF1 mutants, performed biochemical experiments and electron microscopy. S.B and M.H. analyzed the data. S.B. and M.H. wrote the paper with contribution from M.J.S and I.A.

Competing interests

The authors declare no competing interests.

Data availability

EM densities have been deposited in the Electron Microscopy Data Bank under accession codes EMD-21980, EMD-21971, EMD-21970, EMD-21978, EMD-21979, EMD-21981 and EMD-21982. The coordinates of EM-based models have been deposited in the Protein Data Bank under accession codes PDB 6X0N, 6X0L, 6X0M, 6WZ9 and 6WZ5. The RAW data are provided as a Supplementary Fig. file. All other data are available from the corresponding author upon reasonable request.

575 **References**

31. Luger, K., Rechsteiner, T. J., Flaus, A. J., Waye, M. M. & Richmond, T. J. Characterization of nucleosome core particles containing histone proteins made in bacteria. *J. Mol. Biol.* **272**, 301–311 (1997).
32. Bilokapic, S., Strauss, M. & Halic, M. Cryo-EM of nucleosome core particle interactions in trans. *Sci Rep* **8**, 7046 (2018).
33. Bilokapic, S., Strauss, M. & Halic, M. Structural rearrangements of the histone octamer translocate DNA. *Nat Commun* **9**, 1330 (2018).
34. Lowary, P. T. & Widom, J. New DNA sequence rules for high affinity binding to histone octamer and sequence-directed nucleosome positioning. *J. Mol. Biol.* **276**, 19–42 (1998).
35. Bilokapic, S. & Halic, M. Nucleosome and ubiquitin position Set2 to methylate H3K36. *Nat Commun* **10**, 3795 (2019).
36. Zheng, S. Q. *et al.* MotionCor2: anisotropic correction of beam-induced motion for improved cryo-electron microscopy. *Nat. Methods* **14**, 331–332 (2017).
37. Grant, T. & Grigorieff, N. Measuring the optimal exposure for single particle cryo-EM using a 2.6 Å reconstruction of rotavirus VP6. *Elife* **4**, e06980 (2015).
38. Rohou, A. & Grigorieff, N. CTFFIND4: Fast and accurate defocus estimation from electron micrographs. *J. Struct. Biol.* **192**, 216–221 (2015).
39. Wagner, T. *et al.* SPHIRE-crYOLO is a fast and accurate fully automated particle picker for cryo-EM. *Commun Biol* **2**, 218 (2019).
40. Zivanov, J. *et al.* New tools for automated high-resolution cryo-EM structure determination in RELION-3. *Elife* **7**, (2018).
41. Tan, Y. Z. *et al.* Addressing preferred specimen orientation in single-particle cryo-EM through tilting. *Nat. Methods* **14**, 793–796 (2017).
42. Emsley, P., Lohkamp, B., Scott, W. G. & Cowtan, K. Features and development of Coot. *Acta Crystallogr. D Biol. Crystallogr.* **66**, 486–501 (2010).
43. Adams, P. D. *et al.* PHENIX: a comprehensive Python-based system for macromolecular structure solution. *Acta Crystallogr. D Biol. Crystallogr.* **66**, 213–221 (2010).

44. Pettersen, E. F. *et al.* UCSF Chimera--a visualization system for exploratory research and analysis. *J Comput Chem* **25**, 1605–1612 (2004).

Extended Data Fig. 1. Assembly and cryo-EM of PARP2/HPF1 bound to mono-nucleosomes.

a) SDS-PAGE showing the PARP2/HPF1_Nucleosome complex assembly for cryo-EM.

b) Native gel showing the PARP2/HPF1_Nucleosome complex assembly for cryo-EM. Note the shift in the PARP2_Nucleosome complex migration upon binding of HPF1.

c) SDS-PAGE/immunoblotting showing PARP2 PARylation of nucleosomes. HPF1 is required for H3 PARylation.

d) Representative cryo-EM micrograph collected with Titan Krios electron microscope at 300 keV. Bridging of two nucleosomes by PARP2/HPF1 is clearly visible in the raw data. Complex particles in multiple orientations are visible.

e) Representative 2D class averages showing two nucleosomes bridged by PARP2/HPF1. Two nucleosomes are positioned in an almost perpendicular orientation. PARP2/HPF1 density between two nucleosomes is clearly visible. Many details in nuclesomes are visible in 2D class averages.

For gel source data, see Supplementary Fig. 1.

Extended Data Fig. 2. Classification of the PARP2/HPF1_Nucleosome complex.

a) Initial map generated from the entire dataset comprising 934 000 particles. The dataset was further extensively classified. The regions used for focused classifications and refinements in **b-g** are color coded and labeled.

b) Cryo-EM map of Nucleosome 2, refined to 2.2 Å is shown on the left. Fourier shell correlation (FSC) curve showing the resolution of the map (middle). The map is colored by local resolution. The model of the NCP (PDB:6FQ5) was refined into the cryo-EM map. The representative region showing map quality and fit of the model is shown on the right.

c) Angular distribution for Nucleosome 2.

d) Directional FSC plot showing uniform resolution in all directions.

e) Cryo-EM map of Nucleosome 1, refined to 2.8 Å is shown on the left. Fourier shell correlation (FSC) curve showing the resolution of the map (middle). The map is colored by local resolution. The model of the NCP (PDB:6FQ5) was refined into the cryo-EM map. The representative region showing map quality and fit of the model is shown on the right.

f) Focused classification and refinements with focus on connection of the PARP2_WGR domains with the Nucleosome 2 (see **b**). Cryo-EM map of this region was refined to 4.1 Å (left). FSC curve showing the resolution of the map is shown in the middle. The model of the PARP2_WGR domains bound to DNA (PDB:6F5B) was refined into the cryo-EM map. The representative region showing map quality and fit of the model is shown on the right.

g) Focused classification and refinements with focus on connection of the PARP2_WGR domains with the Nucleosome 1 (see **e**). Cryo-EM map of this region was refined to 5.7 Å (left). FSC curve showing the resolution of the map is shown in the middle. The model of the PARP2_WGR domains bound to DNA (PDB:6F5B) was refined into the cryo-EM map. The representative region showing map quality and fit of the model is shown on the right.

Extended Data Fig. 3. Focused classification, refinement and model building: focus on the PARP2/HPF1 complex.

a) The overall dataset comprising 934 000 particles was extensively classified with focus on PARP2/HPF1 complex found in between two nucleosomes.

b) Cryo-EM map of PARP2/HPF1 bound to the nucleosome in the activated conformation. Cryo-EM map of this conformation was refined to 4.2 Å. FSC curve showing the resolution of the map is shown below.

c) Cryo-EM map of PARP2/HPF1 bound to the nucleosome in the open state 1. Cryo-EM map of this conformation was refined to 6.7 Å. FSC curve showing the resolution of the map is shown below. The map is colored by local resolution.

d) Cryo-EM map of PARP2/HPF1 bound to the nucleosome in the open state 2. Cryo-EM map of this conformation was refined to 6.3 Å. FSC curve showing the resolution of the map is shown below. The map is colored by local resolution.

e) The PARP2/HPF1 subset comprising 32 000 particles (left) was further classified and refined. Protruding DNA was eliminated from refinements to improve the resolution. Final map (middle) was refined to 3.9 Å. FSC curve is shown on the right. The map is colored by local resolution.

f) Angular distribution for PARP2/HPF1.

g) Directional FSC plot showing reasonably uniform resolution in all directions.

h) The model of the PARP2_WGR domain (PDB:6F5B), PARP2 catalytic domain (with HD domain) (PDB:4TVJ) and PARP2 catalytic domain (without HD domain) in complex with HPF1 (PDB:6TX3) were refined into the cryo-EM map. The representative regions showing map quality and fit of the model are shown. Side chains are visible in most regions of the map.

Extended Data Fig. 4. PARP2 interaction with nucleosomes.

a) The PARP2/HPF1 subset comprising 140 000 particles (left) was further classified and refined. Final map containing two PARP2/HPF1 (middle) was refined to 6.3 Å. FSC curve is shown on the right. The map is colored by local resolution.

b) Model of activated PARP2/HPF1 (**Fig. 1a**) was rigid body fitted into cryo-EM map of two PARP2/HPF1 complexes bridging two mono-nucleosomes.

c) Schematic representation of PARP2 and HPF1 organization is shown on the left. On the right PARP2/HPF1 model is colored by domains.

d) Map quality and fit of the model is shown for the region shown in **Fig. 1d**.

e) Alignment of PARP2/HPF1 bridging two nucleosomes with 5'-phosphate DNA (PARP2_WGR domains are shown in violet and pink, DNA in grey) with the X-ray structure of isolated PARP2 WGR domains bound to double-strand DNA with 5'-phosphate (yellow, PDB:6F5B).

f) Alignment of PARP2/HPF1 bridging two nucleosomes with 5'-phosphate DNA with the X-ray structure of isolated PARP2 WGR domains bound to double-strand DNA with 5'-phosphate. The model is colored by RMSD.

g) Map quality and fit of the model are shown for the regions shown in **Fig. 1e**.

Extended Data Fig. 5. HPF1 interaction with the nucleosome stabilizes the PARP2/HPF1_Nucleosome complex.

a) Native gel showing the PARP2/HPF1_Nucleosome complex assembly with equimolar amounts of free DNA and nucleosomes. Nucleosomal and free DNA are labeled with Alexa 488. PARP2/HPF1 binds nucleosomes with higher affinity than free DNA.

b) PARP2_Nucleosome and PARP2/HPF1_Nucleosome complex assembly analyzed by EMSA. HPF1 contributes to stability of the complex. Native gel is stained with SYBR Gold.

c) SDS-PAGE showing quality of wild type and mutant HPF1 proteins.

d) PARP2/HPF1_Nucleosome complex assembly with wild type and mutant HPF1 analyzed by EMSA. Mutations in loops that interact with nucleosomal DNA destabilize the complex. Native gel is stained with SYBR Gold.

e) One of PARP2/HPF1 in the map with two PARP2/HPF1 complexes shows flexibility in the N-terminal region of HPF1. Note an additional density spanning from HPF1 to double strand DNA break site. This density could be generated by missing HPF1 helices, HPF1 and the PARP2 N-terminal tail or the H3 tail.

f) Superposition of the PARP2 catalytic domains from the PARP2/HPF1 crystal structure (gray, PDB:6TX3) and the PARP2/HPF1_Nucleosome cryo-EM model (violet and magenta). HPF1 slightly rearranges in the cryo-EM structure when compared to the X-ray structure.

g) Superposition of the PARP2 catalytic domains from the PARP2/HPF1 crystal structure (gray, PDB:6TX3) and the PARP2/HPF1_Nucleosome cryo-EM model. The model is colored by RMSD.

One representative experiment of at least 3 independent experiments is shown for all biochemical data.

For gel source data, see Supplementary Fig. 1.

Extended Data Fig. 6. Bridging two nucleosomes is required for PARP2 activation.

a) PARP2 can bind to double-stranded DNA with 5'-biotin on both ends but can not bridge that DNA. The complex formation was followed on the native gel by staining with SYBR Gold and anti-PARP2 western blot.

b) Native gel showing PARP2 binding to 5 'P and 5 'OH hairpin DNA. This generated two distinct complexes separated on a native gel: PARP2 bound to one DNA and PARP2 bridging two DNAs. PARP2 efficiently bridges hairpin DNA with 5' P, and only weakly DNA with 5' OH. Lanes used for PARylation reaction in **c)** are marked with *.

c) Lanes with equal amounts of PARP2 bridging two DNA from **b)** (marked with *) were incubated with NAD^+ for 7 min to perform in-gel PARylation assay. 2.5x more PARP2 was required to obtain same amount of the bridged complex with 5' OH DNA. PARP2 is activated to the same extent by the bridged 5' P and 5' OH DNA. Only PARP2 bridging two DNAs shows strong ADP-ribosylation activity.

d) SDS-PAGE showing PARP2 auto-PARylation activity. PARP2 was incubated with 5' P and 5' OH hairpin DNA and NAD^+ in solution under conditions from **b)** marked with +. PARP2 is activated more strongly by 5' P hairpin DNA, which forms more stable bridged complex.

e) SDS-PAGE showing quality of wild type and mutant PARP2 proteins.

f) SDS-PAGE showing PARP2 auto-PARylation activity. Wild type and mutant PARP2 were incubated with NAD^+ and with NAD^+ and DNA. Note increased DNA-independent activity of PARP2 mutants, and reduction in DNA-dependent activity.

g) Native gel and anti-H3 Western showing the PARP2_Nucleosome and PARP2/HPF1_Nucleosome complex assembly with wild type and mutant PARP2. Mutations in PARP2 R140 that bridges two nucleosomes abolishes complex formation. Mutation in PARP2 V141 reduces complex stability. Note that complexes with HPF1 show higher stability.

One representative experiment of at least 3 independent experiments is shown for all biochemical data.

For gel source data, see Supplementary Fig. 1.

Extended Data Fig. 7. Bridging two nucleosomes induces conformational changes in PARP2.

a) Alignment of WGR domains of PARP2 cryo-EM model (violet) and PARP1 DNA bound X-ray structure (gray, PDB: 4DQY). Note conformational changes in the CAT_HD domain, especially in helices αA, αB, αF and αG.

b) Alignment of WGR domains of PARP2 cryo-EM model (violet) and PARP1 DNA bound X-ray structure (gray, PDB: 4DQY). The model is colored by RMSD. Note conformational changes in the CAT_HD domain, especially in helices αA, αB, αF and αG.

c) Close-up view of alignment of catalytic ART domains of PARP2 cryo-EM model (violet) and PARP2 catalytic domain X-ray structure (gray, PDB: 4TVJ). Note conformational changes in αB, and the hydrophobic and HD loops.

d) Close-up view of the PARP2 WGR signaling loop interaction with the hydrophobic loop and the HD loop in the HD subdomain. Map quality and fit of the model are shown for the region shown in **Fig**. **2d**. The side chains building the hydrophobic pocket are resolved in the map.

e) Close-up view of PARP2 hydrophobic pocket as in **Fig**. **2e**. The map and the fit of the model are shown for the hydrophobic pocket. Side chains are resolved. The residues building the hydrophobic pocket are labeled.

f) Point mutations in PARP1 and PARP2 showing increase in DNA-independent activity are labeled as red sticks.

g) The map and the fit of the model are shown for the NAD^+ binding site.

Extended Data Fig. 8. Model for the PARP2/HPF1 in the open state 1.

a) Model of activated PARP2/HPF1 bound to nucleosome (**Fig. 1a**) was rigid body fitted into the cryo-EM map of PARP2/HPF1 open state 1 (**Extended Data Fig. 3c**). PARP2 and HPF1 secondary structure elements are resolved in the cryo-EM map and the model can be fitted as rigid body. Model is shown in green and the cryo-EM map in transparent green.

b) Model of PARP2/HPF1 from **a)** is shown fitted into the cryo-EM map. Several PARP2 helices are flexible in this conformation and are not visible in the cryo-EM map. PARP2 helix αE is partially visible at this contour level, and present at lower contour.

c) NAD^+ is shown with the cryo-EM map to depict accessibility to NAD^+ binding site. Flexibility of αD, αF and ASL generates large opening in PARP2, which could allow exchange of NAD^+. NAD^+ (yellow) was modeled based on an alignment with PDB:6BHV.

d) Regions showing increase in hydrogen-deuterium exchange upon PARP1 binding to damaged DNA are shown in red.

e) Comparison of the activated PARP2/HPF1 (violet/magenta) and the open state 1 PARP2/HPF1 (green). Dislocation of PARP2 helices αF, αD and active site loop (ASL) opens the active site for NAD^+ binding. PARP2 helices that are not visible in the PARP2/HPF1 structure in the open state 1 are shown in violet on the right.

f) As in **e)** but close up view at NAD^+ binding site. PARP2 helices that are not visible in the PARP2/HPF1 structure in the open state 1 are shown in violet.

Extended Data Fig. 9. PARP2/HPF1 in the open state 2.

a) Model of the disordered H3 N-terminal tail bound to the active site of the PARP2/HPF1_Nucleosome complex. The H3 tail can reach the composite active site formed by PARP2 and HPF1 (transparent blue).

b) Model of the activated PARP2/HPF1 bound to nucleosome (**Fig. 1a**) was rigid body fitted into the cryo-EM map of PARP2/HPF1 in the open state 2 (**Extended Data Fig. 3d**). PARP2 and HPF1 secondary structure elements are resolved in the cryo-EM map and the model can be fitted as rigid body. Model is shown in blue and the cryo-EM map in transparent blue.

c) Model of PARP2/HPF1 from **b)** is shown fitted into the cryo-EM map. Several PARP2 and HPF1 helices are flexible in this conformation and are not visible in the cryo-EM map.

d) NAD^+ is shown with the cryo-EM map. In this conformation NAD^+ binding site is closed. NAD^+ was modeled based on an alignment with PDB:6BHV.

e) Comparison of the activated PARP2/HPF1 (violet/magenta) and the open state 2 PARP2/HPF1 (blue). Dislocation of PARP2 helices αD and αB, and HPF1 helices α7 and α8, opens potential substrate release pocket.

f) As in **e)** but close up view at NAD^+ binding site. PARP2 helices that are not visible in the PARP2/HPF1 structure in open state 2 are shown in violet.

Extended Data Fig. 10. Mutation that cause resistance to PARP inhibitors.

a) Linker histone H1 is accessible for PARylation while bound to chromatin. Superposition of cryo-EM models of H1-bound nucleosome (gray, PDB:5NL0) and PARP2/HPF1_Nucleosome shows that both complexes can be simultaneously bound to the nucleosome.

b) Model of DNA break recognition by PARP enzymes. Environmental sources and errors in DNA processing enzymes can result in DNA breaks. Poly-ADP ribosylation, post-translation modification deposited by PARP family of enzymes, is the signaling molecule for DNA repair. PARP2 will bind DNA breaks and bridge two broken ends. This changes the conformation of the autoinhibitory HD subdomain and activates the enzyme to ADP-ribosylate histones. ADP-ribosylation, recruits subsequent proteins involved in DNA repair, while PARP/HPF1 remains bound to chromatin. Further increase in PARP automodification releases the complex from chromatin, handing over the repair site to new set of factors.

c) Model of PARP catalytic cycle. Binding and bridging of DNA break induces conformational changes that activate PARP, enabling HPF1 binding. In the first step, the NAD^+ channel needs to open to bind NAD^+. NAD^+ binding closes NAD^+ channel and PARP can add ADP-ribose to target residue. After catalytic reaction is completed, product release channel opens, and product can be released and new substrate can bind.

d) Point mutations and cancer associated SNP variants in PARP1 causing PARP inhibitor resistance are shown as blue sticks.

Extended Data Table 1: Cryo-EM data collection, refinement, and validation statistics

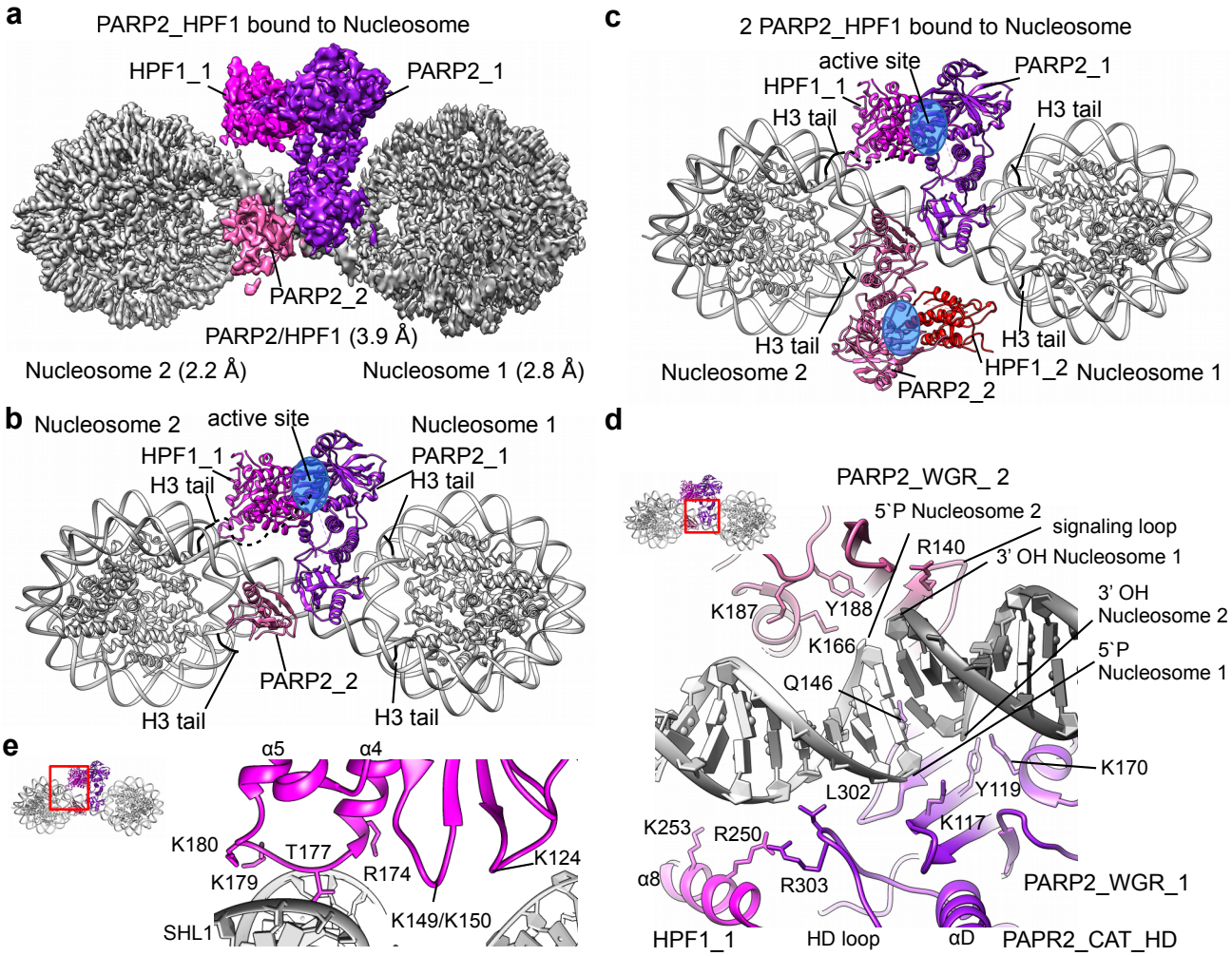
a
PARP2_HPF1 bound to Nucleosome
HPF1_1
PARP2_1
PARP2_2
PARP2/HPF1 (3.9 Å)
Nucleosome 2 (2.2 Å)
Nucleosome 1 (2.8 Å)
c
2 PARP2_HPF1 bound to Nucleosome
active site
HPF1_1
PARP2_1
H3 tail
H3 tail
H3 tail
H3 tail
HPF1_2
Nucleosome 2
Nucleosome 1
PARP2_2
b
Nucleosome 2
active site
Nucleosome 1
HPF1_1
PARP2_1
H3 tail
H3 tail
PARP2_2
H3 tail
H3 tail
d
PARP2_WGR_ 2
5`P Nucleosome 2
signaling loop
R140
3' OH Nucleosome 1
3' OH
Nucleosome 2
K187
Y188
K166
5`P
Nucleosome 1
Q146
K170
L302
Y119
K117
K253
R250
α8
R303
PARP2_WGR_1
HPF1_1
HD loop
αD
PAPR2_CAT_HD
e
α5
α4
K180
T177
K124
K179
R174
SHL1
K149/K150

Figure 1

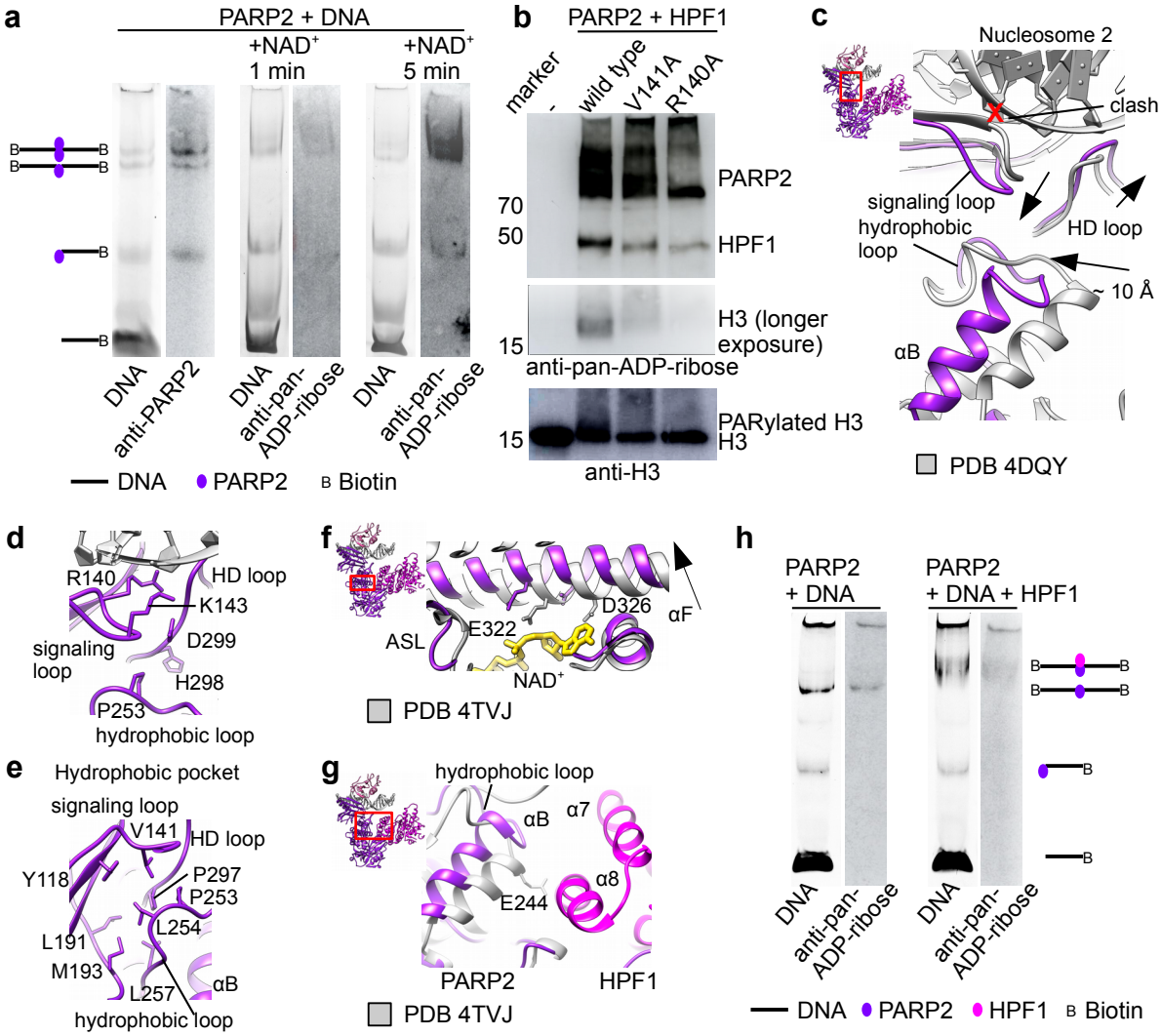
a
PARP2 + DNA
+NAD+ 1 min
+NAD+ 5 min
DNA
anti-PARP2
DNA
anti-pan-ADP-ribose
DNA
anti-pan-ADP-ribose
DNA
PARP2
Biotin
b
PARP2 + HPF1
marker
wild type
V141A
R140A
70
50
PARP2
HPF1
15
H3 (longer exposure)
anti-pan-ADP-ribose
15
PARylated H3
H3
anti-H3
c
Nucleosome 2
clash
signaling loop
hydrophobic loop
HD loop
~ 10 Å
αB
PDB 4DQY
d
R140
HD loop
K143
signaling loop
D299
H298
P253
hydrophobic loop
e
Hydrophobic pocket
signaling loop
V141
HD loop
Y118
P297
P253
L254
L191
M193
L257
αB
hydrophobic loop
f
D326
αF
ASL
E322
NAD+
PDB 4TVJ
g
hydrophobic loop
αB
α7
α8
E244
PARP2
HPF1
PDB 4TVJ
h
PARP2 + DNA
PARP2 + DNA + HPF1
DNA
anti-pan-ADP-ribose
DNA
anti-pan-ADP-ribose
DNA
PARP2
HPF1
Biotin

Figure 2

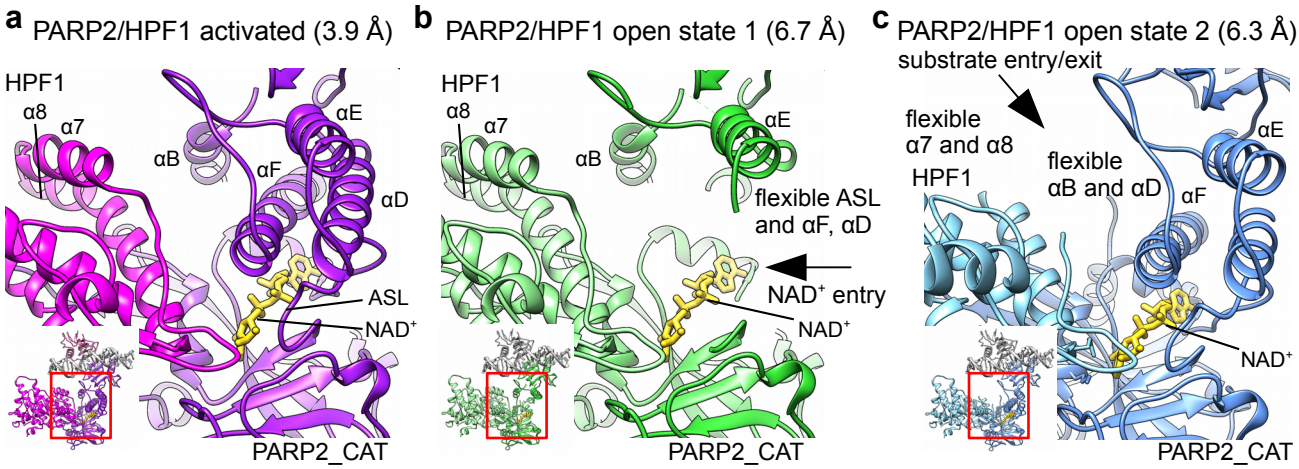
a PARP2/HPF1 activated (3.9 Å)
HPF1
α8
α7
αB
αF
αE
αD
ASL
NAD+
PARP2_CAT
b PARP2/HPF1 open state 1 (6.7 Å)
HPF1
α8
α7
αB
αE
flexible ASL
and αF, αD
NAD+ entry
NAD+
PARP2_CAT
c PARP2/HPF1 open state 2 (6.3 Å)
substrate entry/exit
flexible
α7 and α8
HPF1
flexible
αB and αD
αF
αE
NAD+
PARP2_CAT

Figure 3

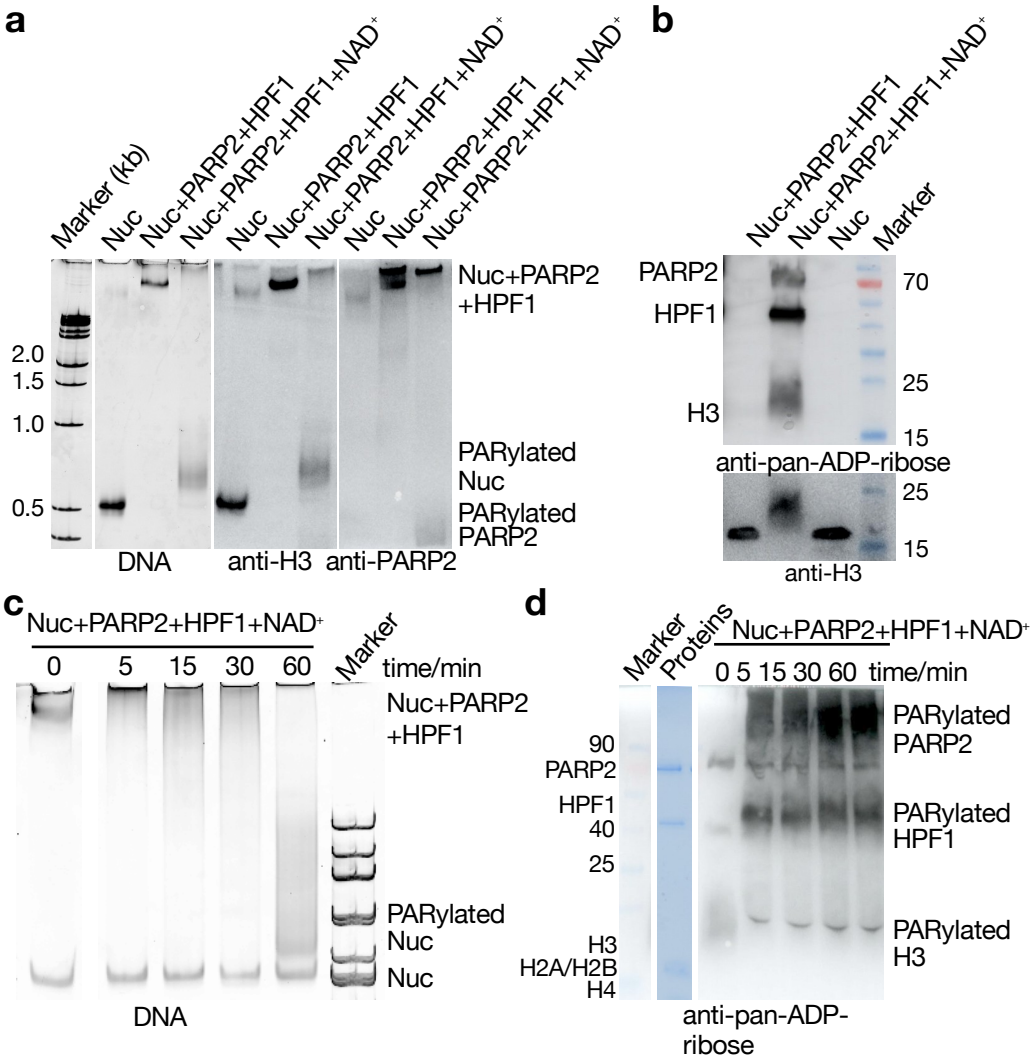
a
Marker (kb)
Nuc
Nuc+PARP2+HPF1
Nuc+PARP2+HPF1+NAD+
Nuc+PARP2
+HPF1
PARylated
Nuc
PARylated
PARP2
2.0
1.5
1.0
0.5
DNA
anti-H3
anti-PARP2
b
PARP2
HPF1
H3
70
25
15
anti-pan-ADP-ribose
anti-H3
c
Nuc+PARP2+HPF1+NAD+
0
5
15
30
60
time/min
Marker
PARylated
Nuc
Nuc
DNA
d
Marker
Proteins
Nuc+PARP2+HPF1+NAD+
0 5 15 30 60 time/min
90
PARP2
HPF1
40
25
H3
H2A/H2B
H4
PARylated
PARP2
PARylated
HPF1
PARylated
H3
anti-pan-ADP-
ribose

Figure 4